

# Comparison of Epoxidation and Baeyer–Villiger Reaction Pathways for Ti(IV)–H<sub>2</sub>O<sub>2</sub> and Sn(IV)–H<sub>2</sub>O<sub>2</sub>

Robert R. Sever and Thatcher W. Root\*

Department of Chemical Engineering, University of Wisconsin-Madison, 1415 Engineering Drive, Madison, Wisconsin 53706

Received: February 8, 2003; In Final Form: June 28, 2003

Density functional theory has been used to study model epoxidation and Baeyer–Villiger reaction mechanisms for Ti(IV)–H<sub>2</sub>O<sub>2</sub> and Sn(IV)–H<sub>2</sub>O<sub>2</sub> catalytic oxidation systems. The titanium and tin catalysts have been modeled with unconstrained single coordination sphere clusters using a B3LYP/ECP methodology. Activation of hydrogen peroxide via formation of a metal hydroperoxo intermediate proceeds with similar energetics over titanium and tin. The overall reaction kinetics for epoxidation of either ethylene or 2,3-dimethyl-1-butene are also similar for Ti(IV)–H<sub>2</sub>O<sub>2</sub> and Sn(IV)–H<sub>2</sub>O<sub>2</sub>. The intrinsic reaction rate for Baeyer–Villiger oxidation of either acetone or 2-methyl-3-pentanone is approximately 5 orders of magnitude slower with Ti(IV)–H<sub>2</sub>O<sub>2</sub> than with Sn(IV)–H<sub>2</sub>O<sub>2</sub>. The greater Lewis acidity of tin relative to titanium enhances adsorption of the ketone substrate on the metal active site and reduces the rate-determining activation barrier for Baeyer–Villiger rearrangement of the chelated Criegee intermediate. These calculations provide insight into experimental results obtained previously for the oxidation of unsaturated ketones with hydrogen peroxide using titanium- and tin-containing redox molecular sieve catalysts.

## Introduction

Redox molecular sieve catalysts have attracted much attention for their potential to perform industrially important oxidation reactions with environmentally benign hydrogen peroxide as oxidant.<sup>1,2</sup> Corma et al.<sup>3</sup> recently announced that tin-containing  $\beta$  zeolite (Sn- $\beta$ ) is a highly active and selective catalyst for Baeyer–Villiger oxidations with hydrogen peroxide. The Baeyer–Villiger reaction is the oxidation of an acyclic or cyclic ketone to an ester or lactone. Esters and lactones are important intermediates and products in a wide range of industries, including the agrochemical, dyestuff, flavor, fragrance, pharmaceutical, and polymer industries. Sn- $\beta$  demonstrated approximately 20 times greater activity than Ti- $\beta$  for Baeyer–Villiger oxidation of cyclohexanone.<sup>4</sup> Sn- $\beta$  yielded 100% lactone selectivities for oxidation of the unsaturated cyclic ketones bicyclo[3.2.0]2-hepten-6-one and dihydrocarvone.<sup>3</sup> Ti- $\beta$ , on the other hand, exclusively catalyzed epoxidation of the double-bond moiety in preference to Baeyer–Villiger oxidation of the carbonyl moiety when tested with dihydrocarvone. To explain the observed chemoselectivity differences between Sn- $\beta$  and Ti- $\beta$ , Corma et al.<sup>3</sup> proposed a Baeyer–Villiger reaction mechanism in which coordination of the ketone substrate on the Lewis acidic metal site activates the carbonyl group for reaction with free hydrogen peroxide. According to this proposal, titanium activates hydrogen peroxide for epoxidation but does not sufficiently activate the carbonyl group for Baeyer–Villiger oxidation with free hydrogen peroxide. Tin conversely activates the carbonyl group for Baeyer–Villiger oxidation but does not sufficiently activate hydrogen peroxide for epoxidation.

Later results obtained by Corma et al.<sup>5</sup> for tin-containing MCM-41 (Sn-MCM-41) catalysts call into question the hypothesis that tin does not activate hydrogen peroxide. The reaction of dihydrocarvone with hydrogen peroxide in the presence of

Sn-MCM-41 yielded lactones with only 68% selectivity, and most side products originated from epoxidation of the double bond. Researchers at the National Chemical Laboratory in Pune, India<sup>6–10</sup> have also investigated the use of tin-containing redox molecular sieves as oxidation catalysts with peroxide oxidants. They reported that tin-containing redox molecular sieves activate hydrogen peroxide for the hydroxylation of aromatic compounds<sup>6–9</sup> and activate *tert*-butyl hydroperoxide for the epoxidation of alkenes.<sup>10</sup>

Other studies have also indicated that titanium-based catalysts perform poorly in Baeyer–Villiger reactions. Bhaumik et al.<sup>11</sup> demonstrated that titanium silicalite-1 (TS-1) catalyzes the Baeyer–Villiger oxidation of cyclohexanone and acetophenone with hydrogen peroxide under biphasic or triphasic reaction conditions, but the activity and ester selectivity were low for all cases. Watanabe et al.<sup>12</sup> also reported that a homogeneous titanium(salen) complex, despite being an excellent sulfoxidation catalyst, possesses little activity for the Baeyer–Villiger oxidation of 3-phenylcyclobutanone with hydrogen peroxide.

On the basis of in situ infrared measurements of cyclohexanone adsorption on Sn- $\beta$  and Ti- $\beta$ , Corma et al.<sup>3</sup> proposed that tin activates the ketone carbonyl group for reaction with free hydrogen peroxide more than titanium. We have previously used quantum chemical calculations to investigate the reaction mechanism for tin-catalyzed Baeyer–Villiger oxidation of the model ketone acetone with hydrogen peroxide.<sup>13</sup> It was shown that a mechanism in which tin exclusively activates the ketone carbonyl cannot explain the rate enhancements achieved with tin-containing redox molecular sieves. Instead, the Baeyer–Villiger oxidation most likely proceeds through reaction pathways in which the ketone substrate and the hydrogen peroxide oxidant both interact with the tin active site. In this study, we use quantum chemical calculations to examine the performance of titanium catalysts for the same model Baeyer–Villiger reaction. Comparison with the tin case helps explain the

\* Corresponding author. E-mail: thatcher@engr.wisc.edu.

experimentally observed superiority of tin-based catalysts for Baeyer–Villiger oxidations with hydrogen peroxide.

It was also shown in our prior investigation that hydrogen peroxide can be activated by tin to form tin hydroperoxo ( $\text{SnOOH}$ ) species.<sup>13</sup> The energetics for the formation of tin hydroperoxo species were shown to be similar to those for titanium hydroperoxo ( $\text{TiOOH}$ ) species. Titanium hydroperoxo species are believed to be the active intermediates in epoxidation reactions catalyzed by titanium-containing redox molecular sieves.<sup>14–18</sup> We have previously used quantum chemical calculations to investigate the reactivity of titanium hydroperoxo species in the epoxidation of the model olefin ethylene with hydrogen peroxide.<sup>19</sup> In the present study, we examine the reactivity of tin hydroperoxo species for the same model epoxidation reaction.

The computational results obtained for model epoxidation and Baeyer–Villiger reactions with  $\text{Ti(IV)}-\text{H}_2\text{O}_2$  and  $\text{Sn(IV)}-\text{H}_2\text{O}_2$  improve fundamental understanding of how the electronic properties of the metal active site control the catalyst performance. The results also offer insights into the selectivities observed by Corma et al.<sup>3</sup> for the oxidation of unsaturated ketones with titanium- and tin-containing redox molecular sieves.

### Computational Methodology

All calculations reported here were performed with Gaussian98<sup>20</sup> and NBO version 5.0<sup>21</sup> software. Density functional theory as implemented in the restricted B3LYP hybrid exchange-correlation scheme was used to include some effects of electron correlation with only a marginal increase in computational cost over Hartree–Fock methods. All results have been obtained for cluster geometries optimized in the gas phase. All stationary points have been characterized with a full vibrational analysis, and all reported energy differences include zero-point energy corrections. Thermochemistry calculations have been performed at 298.15 K and 1 atm to account for entropy effects. The zero-point energy corrections and thermochemistry results ( $\Delta H$ ,  $\Delta S$ , and  $\Delta G$ ) have not been scaled. Titanium and tin were both modeled by a LANL2DZ effective core potential. The LANL2DZ basis set for tin was expanded with additional polarization (d-type) and diffuse (p-type) functions as developed by Check et al.<sup>22</sup> Therefore, titanium and tin have basis sets of comparable size and sophistication with vacant d orbitals available. A 6-311+G(d,p) basis set was used for all other atoms. Natural bond orbital (NBO) methods were used to analyze the resultant wave functions in terms of optimally chosen, localized orbitals corresponding to a Lewis structure representation of chemical bonding.<sup>23</sup> The occupancies of natural bond orbitals are highly condensed in the most important one-center (lone pair) and two-center (bond) members, with electron delocalization effects, or donor–acceptor interactions, treated via standard perturbative techniques.

The titanium and tin active sites were modeled with unconstrained clusters representing the first coordination sphere of the metal center. The simplicity of such a cluster model limits the absolute accuracy of the results reported here with regard to real titanium- and tin-containing redox molecular sieve catalysts. This study seeks to elucidate the important energetic differences between the  $\text{Ti(IV)}-\text{H}_2\text{O}_2$  and  $\text{Sn(IV)}-\text{H}_2\text{O}_2$  catalytic oxidation systems rather than to describe the absolute energetics applicable to any specific titanium- or tin-based catalyst. Any systematic errors arising from the small cluster model should apply to all species and are expected to have a much smaller effect on calculated energy differences. The two

chief sources of potential nonsystematic error for this model are the lack of steric constraints and the alterations in the electronic properties of the metal center and neighboring oxygen atoms caused by cluster truncation. These issues have been addressed in our previous investigations of titanium-catalyzed epoxidation mechanisms<sup>19</sup> and tin-catalyzed Baeyer–Villiger oxidation mechanisms<sup>13</sup> by using constrained, second-coordination sphere cluster models of the metal active sites to check critical results. In all cases, the results obtained with the larger models have shown that trends determined using the single coordination sphere cluster models are reliable. Absolute chemical accuracy may be approached by utilizing embedded cluster methods or constrained multiple coordination sphere cluster models to represent the extended environment of the active site. Such calculations will require substantially larger computational resources but would be justified for an investigation of how particular molecular sieve lattices influence the general reactivity patterns described here.

The titanium and tin active sites in the absence of ligands have been modeled with  $\text{Ti(OH)}_4$  and  $\text{Sn(OH)}_4$  clusters, respectively. These clusters were chosen on the basis of previous experimental characterization of the local metal environment in titanium-<sup>24–31</sup> and tin-containing<sup>3–4,7,32–34</sup> redox molecular sieves. The metal atoms isomorphously substitute for silicon atoms in the molecular sieve framework; they are atomically isolated from one another and tetrahedrally coordinated under vacuum conditions. The metal atoms likely possess two, three, or four  $\text{M}-\text{O}-\text{Si}$  bonds to the siliceous molecular sieve framework, with the remaining tetrahedral metal valencies occupied by hydroxyl groups.<sup>26–29</sup> The hydroxyl groups in our single coordination sphere  $\text{M(OH)}_4$  ( $\text{M} = \text{Ti}$  or  $\text{Sn}$ ) cluster model, therefore, may represent either bonds to framework silicon atoms ( $\text{M}-\text{O}-\text{Si}$  modeled as  $\text{M}-\text{O}-\text{H}$ ) or hydrolyzed framework linkages. We focus our attention on proton-transfer reactions involving the participation of a single hydroxyl group in  $\text{M(OH)}_4$  and treat the other three hydroxyl groups as equivalent, nonreactive structural units. Under liquid-phase reaction conditions, the coordination sphere of the metal center expands to include one or two ligands.<sup>3,4,7,24–26,28,30,34–35</sup> In keeping with the exploratory spirit of this investigation, we have only considered the kinetic or thermodynamic effects of ligand coordination for cases where the ligand directly participates in the reaction mechanism. More information on solvent effects is available in our previous investigations of titanium-catalyzed epoxidation mechanisms<sup>19</sup> and tin-catalyzed Baeyer–Villiger oxidation mechanisms.<sup>13</sup> Ligated clusters will be labeled as  $\text{M(OH)}_4-\text{L}$ , where L is the ligand.

We have studied the activation of hydrogen peroxide on the  $\text{M(OH)}_4$  active site to produce the metal hydroperoxo intermediate  $\text{M(OH)}_3(\text{OOH})$  and the subsequent epoxidation of the model olefin ethylene with that intermediate. We have also examined several potential reaction pathways for the Baeyer–Villiger oxidation of the model ketone acetone with hydrogen peroxide using the  $\text{M(OH)}_4$  and  $\text{M(OH)}_3(\text{OOH})$  active-site models. To better relate the computational results obtained here with the experimental results obtained by Corma et al.<sup>3</sup> for oxidation of the unsaturated ketone dihydrocarvone, we have also calculated activation barriers for the epoxidation and Baeyer–Villiger oxidation of model substrates resembling the local structure of the double bond and carbonyl moieties in dihydrocarvone. As shown in Figure 1, we have chosen 2-methyl-3-pentanone as the model ketone for dihydrocarvone (Figure 1a) and 2,3-dimethyl-1-butene as the model olefin (Figure 1b).

The existence of a single negative vibrational mode was

**TABLE 1. Relative Stabilities of M(OH)<sub>4</sub> Complexes<sup>a</sup>**

M(OH) <sub>4</sub> cluster	$\Delta E$	thermochemistry at 298 K		
		$\Delta H$	$T\Delta S$	$\Delta G$
Ti(OH) <sub>4</sub>	0.0	0.0	0.0	0.0
Ti(OH) <sub>4</sub> –H <sub>2</sub> O	–5.6	–6.9	–11.2	4.3
Ti(OH) <sub>4</sub> –H <sub>2</sub> O <sub>2</sub>	–9.9	–10.8	–12.1	1.3
Ti(OH) <sub>4</sub> –OC(CH <sub>3</sub> ) <sub>2</sub>	–3.8	–4.2	–13.0	8.7
Ti(OH) <sub>4</sub> –OC[CH <sub>2</sub> (CH <sub>3</sub> )] [CH(CH <sub>3</sub> ) <sub>2</sub> ]	–3.9	–4.2	–12.9	8.7
Sn(OH) <sub>4</sub>	0.0	0.0	0.0	0.0
Sn(OH) <sub>4</sub> –H <sub>2</sub> O	–10.9	–12.0	–11.0	–1.0
Sn(OH) <sub>4</sub> –H <sub>2</sub> O <sub>2</sub>	–13.6	–14.2	–11.6	–2.5
Sn(OH) <sub>4</sub> –OC(CH <sub>3</sub> ) <sub>2</sub>	–10.6	–11.0	–13.2	2.3
Sn(OH) <sub>4</sub> –OC[CH <sub>2</sub> (CH <sub>3</sub> )] [CH(CH <sub>3</sub> ) <sub>2</sub> ]	–10.9	–11.0	–13.2	2.2

<sup>a</sup> Energy changes in kcal/mol calculated relative to the nonligated M(OH)<sub>4</sub> cluster and coordinating species at infinite separation.

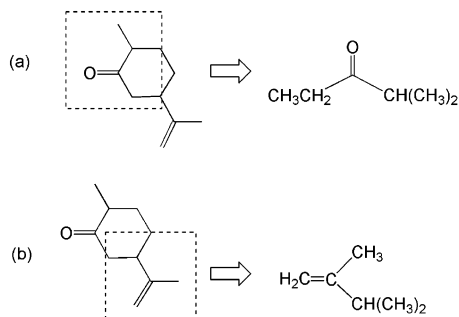


**Figure 1.** (a) The carbonyl group in dihydrocarvone modeled as 2-methyl-3-pentanone, and (b) the double bond in dihydrocarvone modeled as 2,3-dimethyl-1-butene.

confirmed for each optimized transition-state structure, and intrinsic reaction coordinate (IRC) calculations were used to verify the reactants and products corresponding to that mode.<sup>36</sup> Preference is given to the use of the Gibbs free energy of activation over the electronic, or potential, energy of activation as a basis for comparing alternative reaction pathways. The rate constant ( $k$ ) for an elementary reaction step is defined in terms of the Gibbs activation barrier ( $\Delta G_A$ ) as

$$k = \kappa \left( \frac{k_B T}{h} \right) \exp \left( \frac{-\Delta G_A}{RT} \right) = \kappa \left( \frac{k_B T}{h} \right) \exp \left( \frac{\Delta S_A}{R} \right) \exp \left( \frac{-\Delta H_A}{RT} \right) \quad (1)$$

where  $\kappa$  is the transmission coefficient,  $k_B$  is the Boltzmann constant, and  $\Delta S_A$  and  $\Delta H_A$  are the entropic and enthalpic activation barriers, respectively. By incorporating entropy effects, the Gibbs activation barrier provides a more complete representation of intrinsic reaction kinetics at nonzero temperatures than the electronic activation barrier.

## Results and Discussion

**Relative Stabilities of M(OH)<sub>4</sub> Complexes.** Table 1 summarizes the relative stabilities of M(OH)<sub>4</sub> complexes possessing a single ketone, hydrogen peroxide, or water ligand. It is apparent from these results that the tin center is more Lewis acidic than the titanium center and tends to bind ligands more strongly. In particular, the Gibbs free-energy change for coordination of the acetone carbonyl group to the metal center is approximately 6.5 kcal/mol more endothermic for the titanium case than for the tin case. The ligand-binding energies calculated for 2-methyl-3-pentanone, our reduced model of the carbonyl group in dihydrocarvone, are similar to those determined for acetone. In actual redox molecular sieve catalysts, the adsorption strength of ketones larger than acetone may be significantly affected by steric or dispersion interactions between

**TABLE 2. Reaction Energies and Activation Barriers for the Formation of M(OH)<sub>3</sub>(OOH) via the Reaction Mechanism Shown in Figure 2 (all energies in kcal/mol)**

step	Ti				Sn			
	$\Delta E_R$	$\Delta G_R$	$\Delta E_A$	$\Delta G_A$	$\Delta E_R$	$\Delta G_R$	$\Delta E_A$	$\Delta G_A$
1	–9.9	1.3			–13.6	–2.5		
2	2.5	2.3	14.9	15.5	2.8	2.5	14.8	15.4
3	4.3	–5.2			11.3	1.1		

substituents on the carbonyl group and the molecular sieve framework. Assuming that the active sites in titanium- and tin-containing redox molecular sieves possess similar structural environments, the single coordination sphere cluster model used in this study should provide reliable estimates of the relative coordination strength for the carbonyl group on titanium versus tin. The relative binding energies determined in this study are in accordance with the in situ infrared experiments performed by Corma and co-workers,<sup>3,4</sup> which qualitatively showed that cyclohexanone adsorbs more strongly on Sn- $\beta$  than Ti- $\beta$ .

**Formation of Metal Hydroperoxo Intermediates.** The mechanism for the formation of the metal hydroperoxo intermediate M(OH)<sub>3</sub>(OOH) from the M(OH)<sub>4</sub>–H<sub>2</sub>O<sub>2</sub> cluster is shown in Figure 2. The reaction energies ( $\Delta E_R$  and  $\Delta G_R$ ) and activation barriers ( $\Delta E_A$  and  $\Delta G_A$ ) for each elementary step are summarized in Table 2. In the first step, hydrogen peroxide coordinates the metal active site. In step 2, the hydrogen peroxide ligand transfers a hydrogen from the oxygen coordinating the metal center (O $\alpha$ ) to the nearest hydroxyl oxygen (O $\gamma$ ). This proton-transfer step results in the transformation of the coordinated hydrogen peroxide ligand into a hydroperoxo group on the metal and the transformation of a hydroxyl group on the metal into a coordinated water ligand. In the final step, the water ligand desorbs from the metal to yield the nonligated M(OH)<sub>3</sub>–(OOH) intermediate.

The Gibbs activation barriers for proton transfer (step 2, Figure 2) are very similar at 15.5 kcal/mol for titanium and 15.4 kcal/mol for tin. Our previous studies<sup>13,19</sup> showed that localized solvent coordination at the titanium or tin active site invariably lowers the activation barrier for metal hydroperoxo intermediate formation and that the magnitudes of these effects are also similar for titanium and tin. The existence of titanium hydroperoxo species is generally established for many Ti(IV)–H<sub>2</sub>O<sub>2</sub> catalytic oxidation systems, including titanium-containing redox molecular sieves. The similarity of the energetics for tin and titanium suggests that tin hydroperoxo species are also likely to exist for analogous Sn(IV)–H<sub>2</sub>O<sub>2</sub> catalytic oxidation systems under typical reaction conditions.

**Epoxidation.** We have examined epoxidation of the model olefins ethylene and 2,3-dimethyl-1-butene using the Ti(OH)<sub>3</sub>–(OOH) and Sn(OH)<sub>3</sub>(OOH) intermediates as oxygen donors. The

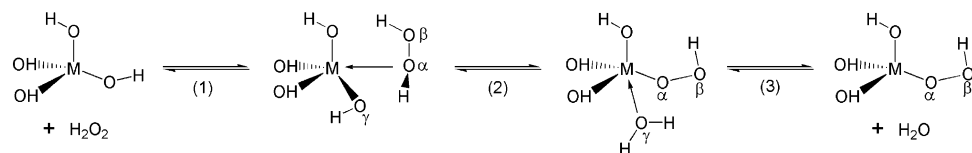


**Figure 2.** Mechanism for the activation of hydrogen peroxide on  $M(OH)_4$  to form the metal hydroperoxo intermediate  $M(OH)_3(OOH)$ . (Structural arrows represent coordinative interactions with the metal.)

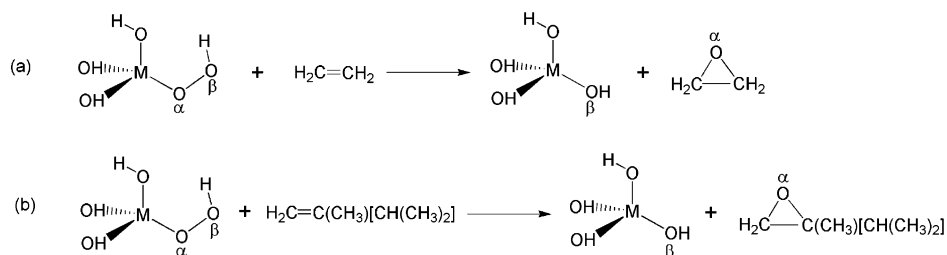


**Figure 3.** The oxygen transfer step in the epoxidation of (a) ethylene and (b) 2,3-dimethyl-1-butene using the hydroperoxo intermediate  $M(OH)_3-(OOH)$ .

**TABLE 3.** Reaction Energies and Activation Barriers<sup>a</sup> for the Epoxidation Reactions Shown in Figure 3 (all energies in kcal/mol)

substrate	Ti				Sn			
	$\Delta E_R$	$\Delta G_R$	$\Delta E_A$	$\Delta G_A$	$\Delta E_R$	$\Delta G_R$	$\Delta E_A$	$\Delta G_A$
ethylene	-44.7	-45.5	14.8	25.7	-48.3	-48.1	9.6	21.3
2,3-dimethyl-1-butene	-49.8	-50.0	10.1	21.4	-53.3	-52.6	5.5	18.0

<sup>a</sup> Calculated as the difference between the energy of the transition state and the energies of the olefin and  $M(OH)_3(OOH)$  reactants at infinite separation.

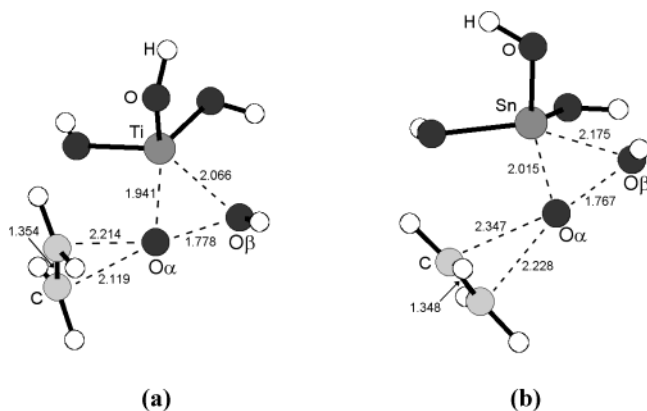


**Figure 4.** Optimized transition-state geometries for the epoxidation of ethylene with (a)  $Ti(OH)_3(OOH)$  and (b)  $Sn(OH)_3(OOH)$ . (Bonds in the process of breaking or forming are shown with dashed lines; bond distances are in Å.)

epoxidation reactions for both substrates are illustrated in Figure 3; the corresponding activation barriers and reaction energies are summarized in Table 3. An oxygen-transfer mechanism was considered in which the alkene double bond attacks the proximal oxygen ( $O\alpha$ ) of the hydroperoxo group in a spiro orientation to the plane containing the metal atom and the hydroperoxo oxygens. The optimized transition states for ethylene epoxidation and 2,3-dimethyl-1-butene epoxidation are shown in Figures 4 and 5, respectively. Transition-state searches were also attempted using an initial planar orientation of ethylene with respect to the MOO plane, but the ethylene molecule invariably optimized into a spiro orientation. Attack of the distal hydroperoxo oxygen ( $O\beta$ ) was not considered to any significant extent because previous studies of titanium-based catalysts<sup>37-39</sup> and our own exploratory calculations<sup>19</sup> have shown proximal attack to be significantly more favored. A stable optimized geometry for the coordination of ethylene directly to the titanium or tin center

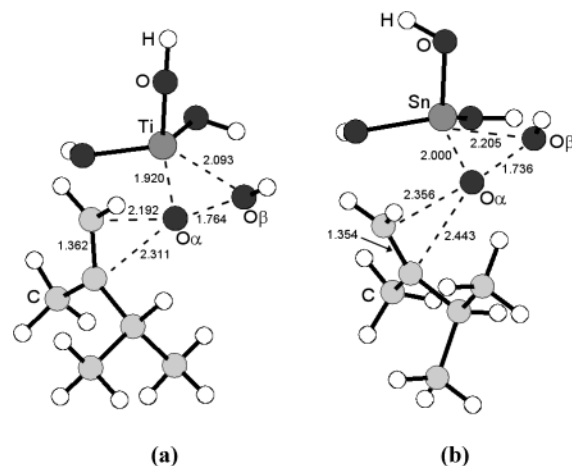


**Figure 5.** Optimized transition-state geometries for the epoxidation of 2,3-dimethyl-1-butene with (a)  $Ti(OH)_3(OOH)$  and (b)  $Sn(OH)_3(OOH)$ . (Bonds in the process of breaking or forming are shown with dashed lines; bond distances are in Å.)

could not be found. Hence, olefin adsorption was not considered as a step in the epoxidation mechanism.

NBO analysis of the transition-state wave functions indicates that the epoxidation reaction follows an electrophilic mechanism in which the  $\pi_{C=C}$  bond of the alkene transfers electrons into the  $\sigma_{O-O}^*$  peroxy antibond of the metal hydroperoxo intermediate. This electron donation dramatically elongates the O—O bond and eventually leads to its cleavage (Figures 4 and 5). In addition to breaking the O—O bond, transfer of the proximal oxygen  $O\alpha$  to the olefin substrate also requires heterolytic cleavage of the M— $O\alpha$  bond and formation of a M— $O\beta$  bond. As a result, the M— $O\alpha$  distance increases in the transition state while the M— $O\beta$  distance decreases. Formation of the M— $O\beta$  bond regenerates the original  $M(OH)_4$  active site (Figure 3).

The Gibbs activation barriers reported in Table 3 are higher than the corresponding electronic activation barriers because



**TABLE 4. Properties of the Peroxo Bond in the Reactant and Transition State Clusters for Epoxidation**

M(OH) <sub>3</sub> (OOH) Reactant				Transition State				
M(OH) <sub>3</sub> (OOH)	atomic charge <sup>a</sup>			olefin reactant	$\Delta G_A^b$	atomic charge <sup>a</sup>		
	O $\alpha$	O $\beta$	M			O $\alpha$	O $\beta$	M
Ti(OH) <sub>3</sub> (OOH)	−0.440	−0.454	1.716	ethylene	25.7	−0.516	−0.675	1.692
Sn(OH) <sub>3</sub> (OOH)	−0.659	−0.496	2.710	ethylene	21.3	−0.674	−0.730	2.748
Ti(OH) <sub>3</sub> (OOH)	−0.440	−0.454	1.716	2,3-dimethyl-1-butene	21.4	−0.518	−0.669	1.691
Sn(OH) <sub>3</sub> (OOH)	−0.659	−0.496	2.710	2,3-dimethyl-1-butene	18.0	−0.678	−0.704	2.750

<sup>a</sup> Atomic charges determined using natural population analysis. <sup>b</sup> Gibbs activation barrier for oxygen transfer in kcal/mol.

of the entropy loss associated with binding the olefin substrate to the metal hydroperoxo oxidant in the transition-state complex. This entropic contribution raises the Gibbs activation barrier for the oxygen transfer step by approximately 11–13 kcal/mol at 298 K.

In both the titanium- and tin-catalyzed epoxidation mechanisms, the Gibbs activation barrier is lower for 2,3-dimethyl-1-butene than for ethylene (Table 3). The activation barrier decreases because the electron-donating alkyl substituents in 2,3-dimethyl-1-butene enhance the nucleophilicity of the double bond and thereby promote its attack of the hydroperoxo moiety. The enhanced nucleophilicity of 2,3-dimethyl-1-butene is reflected in the increase of the  $\pi_{C=C}$  donor orbital energy from −0.7635 Hartree in ethylene to −0.2620 Hartree in 2,3-dimethyl-1-butene (1 Hartree = 627.5 kcal/mol). A similar effect of alkene branching on epoxidation activation barriers has been observed previously for related electrophilic oxidants, such as peroxyformic acid<sup>40</sup> and molybdenum<sup>41,42</sup> and rhenium<sup>42</sup> bisperoxo complexes.

The Gibbs activation barriers for epoxidation of ethylene and 2,3-dimethyl-1-butene with Sn(OH)<sub>3</sub>(OOH) are approximately 3.4–4.4 kcal/mol less than the corresponding barriers for Ti(OH)<sub>3</sub>(OOH). NBO analysis indicates that the  $\sigma_{O-O}^*$  antibond orbital in the epoxidation transition state is polarized toward the proximal hydroperoxo oxygen O $\alpha$  to promote the  $\pi_{C=C} \rightarrow \sigma_{O-O}^*$  donor–acceptor interaction with the olefin substrate. The  $\sigma_{O-O}$  bond orbital is concomitantly polarized toward the distal hydroperoxo oxygen O $\beta$ , and as a result, O $\beta$  gains substantial negative charge in the transition state as shown in Table 4. The developing negative charge on O $\beta$  is stabilized by interaction with the electronegative and positively charged metal center. One can see from Table 4 that the tin center is much more positively charged than the titanium center. NBO analysis reveals that the lone pair electrons on the oxygen atoms bonded to the titanium center donate substantial electron charge back into the empty valence 3d orbitals of titanium. As a result, the titanium center becomes less positively charged and its Lewis acidity is partially quenched. Such back-donation of electrons from the hydroxyl oxygens does not occur for the tin center because the valence 4d orbitals of tin are filled. The greater electrostatic stabilization of the transition state provided by the more positively charged tin center reduces the activation barrier for epoxidation with Sn(OH)<sub>3</sub>(OOH) relative to Ti(OH)<sub>3</sub>(OOH).

In all cases considered here, the activation barrier for oxygen transfer from the metal hydroperoxo intermediate (Table 3) is greater than the activation barrier for its formation (Table 2). The oxygen transfer step therefore represents the rate-determining step of the overall epoxidation mechanism. The overall rate constant ( $k_{\text{overall}}$ ) for a reaction pathway with an irreversible rate-determining step can be accurately approximated as

$$k_{\text{overall}} = \kappa \left( \frac{k_B T}{h} \right) \exp \left( \frac{-\Delta G_{\text{total}}}{RT} \right) \quad (2)$$

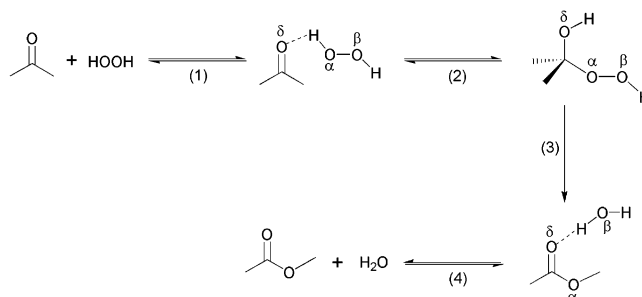
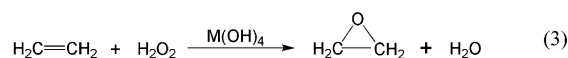


**Figure 6.** Mechanism for the noncatalyzed Baeyer–Villiger oxidation of acetone with hydrogen peroxide. (Dashed lines represent hydrogen-bonding interactions.)

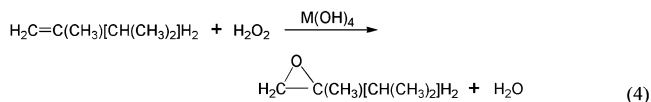
**TABLE 5. Reaction Energies and Activation Barriers for the Noncatalyzed Baeyer–Villiger Oxidation of Acetone with Hydrogen Peroxide via the Reaction Mechanism Shown in Figure 6 (all energies in kcal/mol)**

step	noncatalyzed			
	$\Delta E_R$	$\Delta G_R$	$\Delta E_A$	$\Delta G_A$
1	−6.6	2.1		
2	1.8	5.0	37.3	39.8
3	−70.0	−72.8	41.7	41.7
4	4.2	−4.3		

where the transmission coefficient  $\kappa$  is of order one and  $\Delta G_{\text{total}}$  is the sum of the Gibbs activation barrier for the rate-determining step and the Gibbs free energy changes of reaction for all the preceding quasi-equilibrated steps. The overall reaction



proceeds with  $\Delta G_{\text{total}} = 24.1$  kcal/mol over Ti(OH)<sub>4</sub> and  $\Delta G_{\text{total}} = 22.4$  kcal/mol over Sn(OH)<sub>4</sub>. The overall reaction



proceeds with  $\Delta G_{\text{total}} = 19.8$  kcal/mol over Ti(OH)<sub>4</sub> and  $\Delta G_{\text{total}} = 19.1$  kcal/mol over Sn(OH)<sub>4</sub>. Thus, the overall reaction rate constants for ethylene epoxidation and 2,3-dimethyl-1-butene epoxidation are similar for titanium and tin catalysts. These results therefore suggest that the Sn(IV)–H<sub>2</sub>O<sub>2</sub> catalytic oxidation system should be as intrinsically capable as the Ti(IV)–H<sub>2</sub>O<sub>2</sub> system of performing epoxidation reactions.

**Baeyer–Villiger Oxidation.** The noncatalyzed Baeyer–Villiger reaction mechanism provides a useful basis of comparison for the metal-catalyzed routes. The generally accepted mechanism is shown in Figure 6;<sup>43–46</sup> the calculated reaction energies and activation barriers for each elementary step are reported in Table 5. In the first step, hydrogen peroxide donates a hydrogen bond to the carbonyl oxygen (O $\delta$ ). In step 2, hydrogen peroxide adds across the carbonyl double bond to

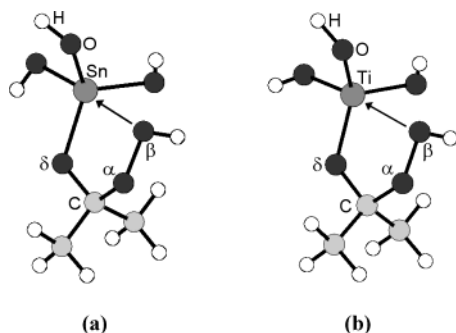


**Figure 7.** Optimized geometries of the chelated Criegee intermediates: (a)  $\text{Sn}(\text{OH})_3[\text{OC}(\text{OOH})(\text{CH}_3)_2]$  and (b)  $\text{Ti}(\text{OH})_3[\text{OC}(\text{OOH})(\text{CH}_3)_2]$ . (Arrow represents coordinative interaction with the metal center.)

**TABLE 6. Reaction Energies and Activation Barriers for the Formation of the Chelated Criegee Intermediate  $\text{M}(\text{OH})_3[\text{OC}(\text{OOH})(\text{CH}_3)_2]$  via Mechanism I Shown in Figure 8 (all energies in kcal/mol)**

step	Ti				Sn			
	$\Delta E_R$	$\Delta G_R$	$\Delta E_A$	$\Delta G_A$	$\Delta E_R$	$\Delta G_R$	$\Delta E_A$	$\Delta G_A$
1	-3.8	8.7			-10.6	2.3		
2	-9.9	-0.4			-8.1	1.2		
3	4.6	7.8	11.6	14.4	3.9	7.3	7.9	11.1
4	1.5	-8.0			5.3	-4.3		

generate a tetrahedral  $\text{C}(\text{OH})(\text{OOH})(\text{CH}_3)_2$  species called the “Criegee” intermediate. In step 3, the Criegee intermediate undergoes irreversible Baeyer–Villiger rearrangement to yield methyl acetate with the water-leaving group hydrogen bonded to the carbonyl oxygen. In the final step, the methyl acetate and water products separate. The high activation barriers determined for the noncatalyzed mechanism are in accordance with the experimental observation that Baeyer–Villiger oxidation of ketones with hydrogen peroxide does not occur to any significant extent without catalytic activation.

In a previous investigation,<sup>13</sup> we examined several possible reaction mechanisms for tin-catalyzed Baeyer–Villiger oxidation of acetone with hydrogen peroxide. We considered a reaction mechanism similar to the one proposed by Corma et al.<sup>3</sup> They suggested that coordination of the ketone substrate at the Lewis acidic metal site activates the carbonyl group for reaction with free hydrogen peroxide. This reaction mechanism is exactly analogous to the noncatalyzed mechanism (Figure 6), the only difference being the coordination of the ketone substrate and Criegee intermediate to the metal active site during

steps 2 and 3. This mechanism was determined to be highly unlikely for tin because the activation barriers for formation and rearrangement of the Criegee intermediate remained high at 38.4 and 35.7 kcal/mol, respectively. Investigation of the same mechanism for the titanium case indicates that the activation barrier for the Baeyer–Villiger rearrangement step is likewise high at 39.7 kcal/mol. As a result, this mechanism has not been studied further for titanium.

The tin-catalyzed Baeyer–Villiger oxidation of acetone with hydrogen peroxide was shown<sup>13</sup> to proceed through the “chelated” Criegee intermediate  $\text{Sn}(\text{OH})_3[\text{OC}(\text{OOH})(\text{CH}_3)_2]$  presented in Figure 7a. In this species, the original carbonyl oxygen ( $\text{O}\delta$ ) of the acetone substrate bonds to the tin center while the distal hydroperoxy oxygen ( $\text{O}\beta$ ) coordinates the tin center. It was discovered that the  $\text{Sn}(\text{OH})_3[\text{OC}(\text{OOH})(\text{CH}_3)_2]$  intermediate can form via three different pathways, although only two of those pathways are energetically probable for tin. The same three pathways have been considered for the case of titanium. The reaction mechanisms are described briefly below. The results obtained for titanium during this investigation are summarized and compared with the results obtained previously for tin. For the most part, only titanium structures are shown; the corresponding tin structures are very similar and have been presented previously.<sup>13</sup>

In mechanism I, the metal active site directly participates in the addition reaction between hydrogen peroxide and acetone. This mechanism is shown in Figure 8; the reaction energies and activation barriers for each elementary step are reported in Table 6. In the first two steps, acetone coordinates the metal center and hydrogen peroxide donates a hydrogen bond to one of the hydroxyl oxygens ( $\text{O}\gamma$ ) on the metal. In step 3, the hydrogen peroxide oxygen  $\text{O}\alpha$  nucleophilically attacks the carbonyl carbon while the hydroxyl oxygen  $\text{O}\gamma$  simultaneously abstracts the hydrogen-bonded proton from hydrogen peroxide. Attack of the carbonyl carbon proceeds through a  $\text{nO}\alpha \rightarrow \pi_{\text{C}=\text{O}\delta}^*$  donor–acceptor interaction. As a result of this interaction, the carbonyl  $\pi$ -bond is broken, and the carbonyl oxygen  $\text{O}\delta$  forms a bond with the metal. The proton-transfer reaction between  $\text{O}\alpha$  and  $\text{O}\gamma$  transforms the hydroxyl group on the metal into a water ligand. The transition state for this concerted reaction step is shown for the case of titanium in Figure 9. The net result of step 3 is the formation of the chelated Criegee intermediate  $\text{M}(\text{OH})_3[\text{OC}(\text{OOH})(\text{CH}_3)_2]$  with a single water ligand on the metal center. Loss of the water ligand yields the nonligated  $\text{M}(\text{OH})_3[\text{OC}(\text{OOH})(\text{CH}_3)_2]$  intermediate (step 4). The optimized

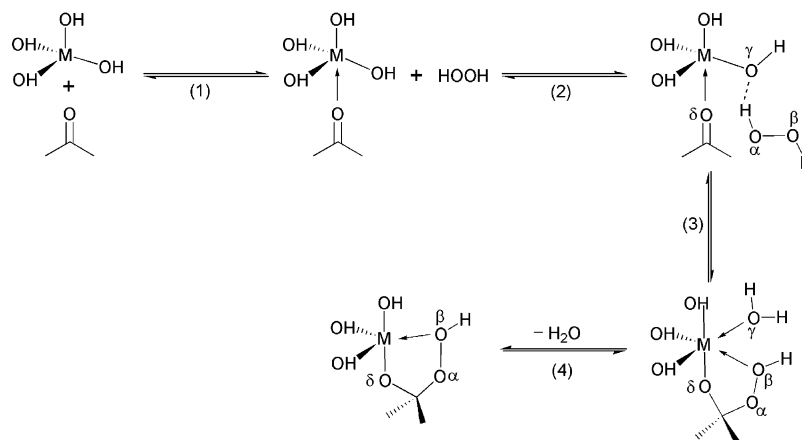


**Figure 8.** Mechanism I for the formation of the chelated Criegee intermediate  $\text{M}(\text{OH})_3[\text{OC}(\text{OOH})(\text{CH}_3)_2]$ . Hydrogen peroxide attacks the carbonyl carbon in acetone and simultaneously transfers a proton to a hydroxyl group oxygen in  $\text{M}(\text{OH})_4$ . (Structural arrows represent coordinative interactions with the metal; dashed lines represent hydrogen-bonding interactions.)

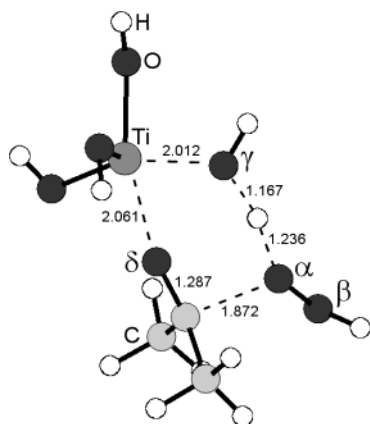


**Figure 9.** Optimized transition-state geometry for the formation of the chelated Criegee intermediate  $\text{Ti}(\text{OH})_3[\text{OC}(\text{OOH})(\text{CH}_3)_2] \cdot \text{H}_2\text{O}$  via step 3 in mechanism I. (Bonds in the process of breaking or forming are shown with dashed lines; bond distances are in Å.)

**TABLE 7. Reaction Energies and Activation Barriers for the Formation of the Chelated Criegee Intermediate  $\text{M}(\text{OH})_3[\text{OC}(\text{OOH})(\text{CH}_3)_2]$  via Mechanism II Shown in Figure 10 (all energies in kcal/mol)**

step	Ti				Sn			
	$\Delta E_R$	$\Delta G_R$	$\Delta E_A$	$\Delta G_A$	$\Delta E_R$	$\Delta G_R$	$\Delta E_A$	$\Delta G_A$
1	−3.0	9.3			−10.7	2.3		
2	−1.5	0.3	11.8	13.2	0.8	3.1	11.9	13.7

geometry of the  $\text{Ti}(\text{OH})_3[\text{OC}(\text{OOH})(\text{CH}_3)_2]$  intermediate is shown in Figure 7b.

Mechanism II for the formation of the chelated Criegee intermediate is shown in Figure 10; the reaction energies and activation barriers for each elementary step are reported in Table 7. In the first step, acetone coordinates the metal center of the metal hydroperoxo intermediate  $\text{M}(\text{OH})_3(\text{OOH})$ . The  $\text{M}(\text{OH})_3(\text{OOH})$  species is generated by the reaction of hydrogen peroxide on the original  $\text{M}(\text{OH})_4$  active site in accordance with the mechanism presented earlier in Figure 2 (see energetics in Table 2). In step 2, the hydroperoxo group attacks the carbonyl carbon to yield the chelated Criegee intermediate  $\text{M}(\text{OH})_3[\text{OC}(\text{OOH})(\text{CH}_3)_2]$ . A lone pair on the proximal hydroperoxo oxygen  $\text{O}_\alpha$  donates electrons into the  $\pi_{\text{C}=\text{O}}^*$  antibond orbital of the carbonyl group. As a result, the carbonyl  $\pi$ -bond heterolytically cleaves, and the carbonyl oxygen  $\text{O}_\delta$  forms a bond with the metal center. A new bond also forms between the attacking  $\text{O}_\alpha$  and the carbonyl carbon while the original bond between the metal center and  $\text{O}_\alpha$  breaks. The transition state for step 2 is shown for the case of titanium in Figure 11.

In mechanism III for the formation of the chelated Criegee intermediate, the metal hydroperoxo species  $\text{M}(\text{OH})_3(\text{OOH})$  behaves like a peracid. This mechanism is presented in Figure 12; the reaction energies and activation barriers for each elementary step are reported in Table 8. In the first step, the hydroperoxo moiety in  $\text{M}(\text{OH})_3(\text{OOH})$  donates a hydrogen bond to the carbonyl oxygen of acetone. In step 2, the hydroperoxo group adds across the carbonyl double bond. The carbonyl

oxygen  $\text{O}_\delta$  abstracts the proton from the distal hydroperoxo oxygen  $\text{O}_\beta$  via a  $\text{n}_{\text{O}_\delta} \rightarrow \sigma_{\text{O}_\beta-\text{H}}^*$  donor–acceptor interaction while the proximal hydroperoxo oxygen  $\text{O}_\alpha$  simultaneously attacks the carbonyl carbon via a  $\text{n}_{\text{O}_\alpha} \rightarrow \pi_{\text{C}=\text{O}}^*$  interaction. During this addition reaction, the  $\text{M}-\text{O}_\alpha$  bond breaks, and a new  $\text{M}-\text{O}_\beta$  bond forms. The transition state for step 2 is shown for the case of titanium in Figure 13a. The end result of step 2 is the formation of the new chelated Criegee intermediate  $\text{M}(\text{OH})_3[\text{OOC}(\text{OH})(\text{CH}_3)_2]$  shown schematically in Figure 12. This intermediate differs from the  $\text{M}(\text{OH})_3[\text{OC}(\text{OOH})(\text{CH}_3)_2]$  intermediate shown in Figure 7 by having a formal bond between the metal and the peroxo group and a coordinative interaction between the metal and the original carbonyl oxygen  $\text{O}_\delta$ . The  $\text{M}(\text{OH})_3[\text{OOC}(\text{OH})(\text{CH}_3)_2]$  intermediate may rearrange to produce methyl acetate, but the activation barrier for this process was calculated to be very high ( $\Delta G_A = 44.8$  kcal/mol) in the case of tin. The  $\text{M}(\text{OH})_3[\text{OOC}(\text{OH})(\text{CH}_3)_2]$  Criegee intermediate may alternatively rearrange via step 3 in Figure 12 to produce the  $\text{M}(\text{OH})_3[\text{OC}(\text{OOH})(\text{CH}_3)_2]$  intermediate. Proton donation from  $\text{O}_\delta$  to  $\text{O}_\beta$  leads to the formation of a new bond between the metal and  $\text{O}_\delta$  and the cleavage of the bond between the metal and  $\text{O}_\beta$ . The transition state for step 3 is shown for the case of titanium in Figure 13b.

The chelated Criegee intermediate  $\text{M}(\text{OH})_3[\text{OC}(\text{OOH})(\text{CH}_3)_2]$  generated via mechanism I, II, or III rearranges to produce the methyl acetate product. The elementary steps for this process are presented in Figure 14; the reaction energies and activation barriers are reported in Table 9. In the Baeyer–Villiger rearrangement step (step 1), the  $\text{O}-\text{O}$  peroxo bond heterolytically cleaves to permit transfer of the proximal oxygen  $\text{O}_\alpha$  to the migrating methyl group and transfer of the distal oxygen  $\text{O}_\beta$  to the metal center. The primary donor–acceptor interaction causing cleavage of the peroxo bond is a donation from the  $\sigma_{\text{C}-\text{O}}$  bonding orbital of the migrating carbon into the  $\sigma_{\text{O}-\text{O}}^*$  antibond orbital. The  $\text{M}-\text{O}_\delta$  bond simultaneously breaks, and the carbonyl group reforms. The optimized transition state for step 1 is shown for the case of titanium in Figure 15. The net result of step 1 is formation of the methyl acetate product coordinated to the metal center and regeneration of the  $\text{M}(\text{OH})_4$  active site. In the final step of the overall Baeyer–Villiger mechanism, the methyl acetate product desorbs from the metal active site.

The Gibbs activation barriers for Baeyer–Villiger rearrangement of the chelated Criegee intermediates  $\text{Sn}(\text{OH})_3[\text{OC}(\text{OOH})(\text{CH}_3)_2]$  and  $\text{Ti}(\text{OH})_3[\text{OC}(\text{OOH})(\text{CH}_3)_2]$  (Table 9) are much lower than the corresponding activation barrier for the noncatalyzed mechanism (Table 2). The Baeyer–Villiger rearrangement of the chelated Criegee intermediate  $\text{M}(\text{OH})_3[\text{OC}(\text{OOH})(\text{CH}_3)_2]$  is facilitated by the coordinative interaction between the distal hydroperoxo oxygen  $\text{O}_\beta$  and the metal center. NBO analysis indicates that the  $\sigma_{\text{O}-\text{O}}^*$  antibond orbital in the Baeyer–Villiger transition state is polarized toward the proximal hydroperoxo oxygen  $\text{O}_\alpha$  to promote the  $\sigma_{\text{C}-\text{O}} \rightarrow \sigma_{\text{O}-\text{O}}^*$  donor–acceptor interaction with the migrating carbon. The  $\sigma_{\text{O}-\text{O}}$  bond orbital is concomitantly polarized toward the distal hydroperoxo oxygen

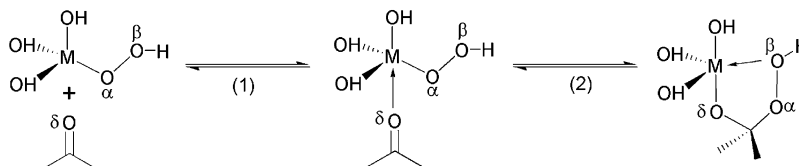


**Figure 10.** Mechanism II for the formation of the chelated Criegee intermediate  $\text{M}(\text{OH})_3[\text{OC}(\text{OOH})(\text{CH}_3)_2]$ . Acetone is coordinated to  $\text{M}(\text{OH})_3(\text{OOH})$  and reacts with the metal hydroperoxo group. (Structural arrows represent coordinative interactions with the metal.)

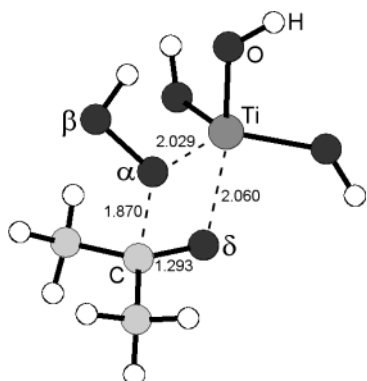


**Figure 11.** Optimized transition-state geometry for the formation of the chelated Criegee intermediate  $\text{Ti}(\text{OH})_3[\text{OC}(\text{OOH})(\text{CH}_3)_2]$  via step 2 in mechanism II. (Bonds in the process of breaking or forming are shown with dashed lines; bond distances are in Å.)

**TABLE 8. Reaction Energies and Activation Barriers for the Formation of the Chelated Criegee Intermediate  $\text{M}(\text{OH})_3[\text{OC}(\text{OOH})(\text{CH}_3)_2]$  via Mechanism III Shown in Figure 12 (all energies in kcal/mol)**

step	Ti				Sn			
	$\Delta E_R$	$\Delta G_R$	$\Delta E_A$	$\Delta G_A$	$\Delta E_R$	$\Delta G_R$	$\Delta E_A$	$\Delta G_A$
1	-8.7	2.4			-7.9	2.0		
2	4.8	6.1	16.4	18.8	-2.7	2.6	21.0	24.1
3	-0.6	1.2	23.4	25.8	0.7	0.8	30.4	30.8

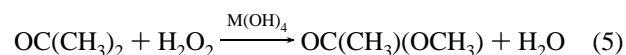
**TABLE 9. Reaction Energies and Activation Barriers for the Rearrangement of the Chelated Criegee Intermediate  $\text{M}(\text{OH})_3[\text{OC}(\text{OOH})(\text{CH}_3)_2]$  via the Reaction Mechanism Shown in Figure 14 (all energies in kcal/mol)**

step	Ti				Sn			
	$\Delta E_R$	$\Delta G_R$	$\Delta E_A$	$\Delta G_A$	$\Delta E_R$	$\Delta G_R$	$\Delta E_A$	$\Delta G_A$
1	-66.6	-68.3	29.9	29.5	-69.7	-71.3	24.7	24.1
2	3.5	-9.8			8.4	-5.1		

$\text{O}\beta$ , and as a result,  $\text{O}\beta$  gains substantial negative charge in the transition state as shown in Table 10. The highly electronegative and positively charged metal atom stabilizes the developing negative charge on the distal hydroperoxy oxygen  $\text{O}\beta$  in the transition state. This electrostatic stabilization reduces the energy of the transition state for Baeyer–Villiger rearrangement of the chelated Criegee intermediates relative to the nonchelated intermediate and thereby reduces the calculated activation barriers. In the noncatalyzed mechanism, water is the leaving

group for heterolytic cleavage of the peroxo bond; in the metal-catalyzed mechanisms, however, the leaving group is essentially  $\text{MOH}$ . As was seen for the case of epoxidation, tin is better capable of stabilizing the negative charge on the distal hydroperoxy oxygen because the Lewis acidity of titanium is partially quenched via back-donation of the lone pair electrons on the hydroxyl group oxygens into titanium's empty valence d shell. As a result, the activation barrier for Baeyer–Villiger rearrangement of  $\text{Sn}(\text{OH})_3[\text{OC}(\text{OOH})(\text{CH}_3)_2]$  is 5.4 kcal/mol lower than the barrier for  $\text{Ti}(\text{OH})_3[\text{OC}(\text{OOH})(\text{CH}_3)_2]$ .

The Gibbs activation barrier for the irreversible Baeyer–Villiger rearrangement of the chelated Criegee intermediate  $\text{Ti}(\text{OH})_3[\text{OC}(\text{OOH})(\text{CH}_3)_2]$  is much greater than the activation barriers for its formation via mechanisms I, II, or III. Baeyer–Villiger rearrangement is therefore the rate-determining step for all three titanium-catalyzed mechanisms. Assuming quasi-equilibration of all steps preceding the rate-determining step, the overall reaction kinetics will be the same for the three mechanisms. The overall rate constant for the Baeyer–Villiger reaction can be approximated once again with eq 2. The overall reaction



proceeds with  $\Delta G_{\text{total}} = 37.6$  kcal/mol over the  $\text{Ti}(\text{OH})_4$  active site.

In the case of tin, Baeyer–Villiger rearrangement of the chelated Criegee intermediate  $\text{Sn}(\text{OH})_3[\text{OC}(\text{OOH})(\text{CH}_3)_2]$  is also the rate-determining step for mechanisms I and II. As a result, the tin-catalyzed mechanisms I and II are kinetically indistinguishable with  $\Delta G_{\text{total}} = 30.6$  kcal/mol. The rate-determining step for mechanism III, however, is the rearrangement of the  $\text{Sn}(\text{OH})_3[\text{OOC}(\text{OH})(\text{CH}_3)_2]$  intermediate to the  $\text{Sn}(\text{OH})_3[\text{OC}(\text{OOH})(\text{CH}_3)_2]$  intermediate (step 3, Figure 12). The activation barrier for this step alone is 30.8 kcal/mol, and the value of  $\Delta G_{\text{total}}$  for the complete mechanism is 36.5 kcal/mol. Hence, the tin-catalyzed Baeyer–Villiger oxidation of acetone with hydrogen peroxide will most likely proceed through either mechanism I or II.

We have also investigated the Baeyer–Villiger oxidation of 2-methyl-3-pentanone with hydrogen peroxide via mechanism II. The reaction energies and activation barriers for the complete mechanism are provided in Table 11. The rate-determining step for the oxidation of 2-methyl-3-pentanone using both tin and

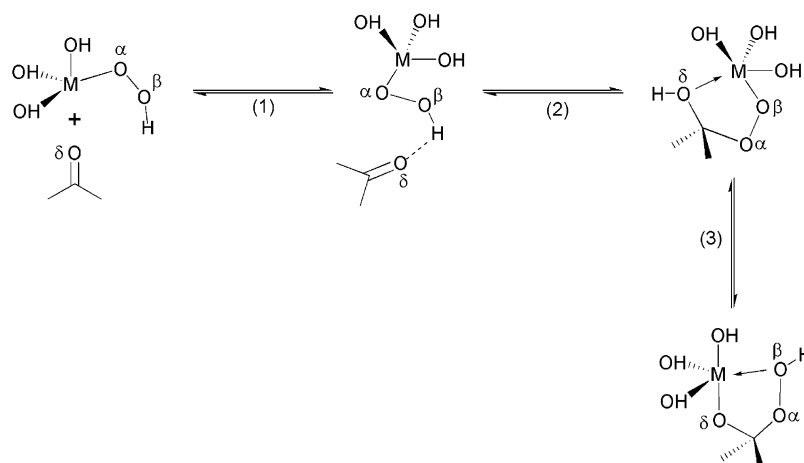


**Figure 12.** Mechanism III for the formation of the chelated Criegee intermediate  $\text{M}(\text{OH})_3[\text{OC}(\text{OOH})(\text{CH}_3)_2]$ . The metal hydroperoxide species acts like a peracid and adds across the carbonyl double bond of the noncoordinated acetone reactant. (Structural arrows represent coordinative interactions with the metal; dashed lines represent hydrogen-bonding interactions.)



**TABLE 10. Atomic Charge Analysis<sup>a</sup> for the Baeyer–Villiger Rearrangement of the Criegee Intermediate**

	Criegee Intermediate				Transition State		
	atomic charge			$\Delta G_A^c$	atomic charge		
	O $\alpha$	O $\beta$	M/H <sup>b</sup>		O $\alpha$	O $\beta$	M/H <sup>b</sup>
HOC(OOH)(CH <sub>3</sub> ) <sub>2</sub>	−0.347	−0.473	0.469	41.7	−0.358	−0.706	0.484
Ti(OH) <sub>3</sub> [OC(OOH)(CH <sub>3</sub> ) <sub>2</sub> ]	−0.322	−0.425	1.705	29.5	−0.342	−0.772	1.689
Sn(OH) <sub>3</sub> [OC(OOH)(CH <sub>3</sub> ) <sub>2</sub> ]	−0.320	−0.488	2.732	24.1	−0.340	−0.884	2.731

<sup>a</sup> Atomic charges determined using natural population analysis. <sup>b</sup> Charge on the atom (Ti, Sn, or H) that bonds with the distal oxygen O $\beta$  to form the leaving group when the peroxo bond is cleaved. <sup>c</sup> Gibbs activation barrier for Baeyer–Villiger rearrangement in kcal/mol.

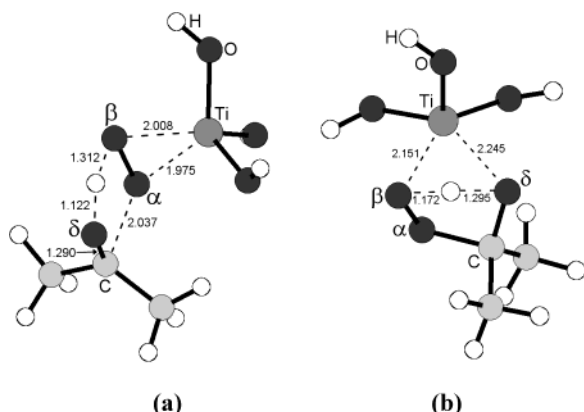


**Figure 13.** Optimized transition-state geometry for the formation of the chelated Criegee intermediates (a) Ti(OH)<sub>3</sub>[OOC(OH)(CH<sub>3</sub>)<sub>2</sub>] via step 2 in mechanism III and (b) Ti(OH)<sub>3</sub>[OC(OOH)(CH<sub>3</sub>)<sub>2</sub>] via step 3 in mechanism III. (Bonds in the process of breaking or forming are shown with dashed lines; bond distances are in Å.)

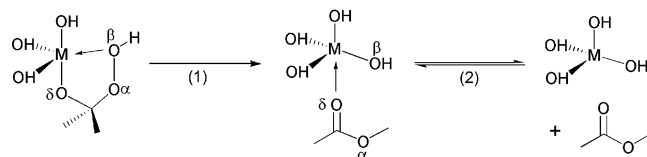


**Figure 14.** Mechanism for the Baeyer–Villiger rearrangement of the chelated Criegee intermediate M(OH)<sub>3</sub>[OC(OOH)(CH<sub>3</sub>)<sub>2</sub>] to yield the methyl acetate product. (Structural arrows represent coordinative interactions with the metal.)

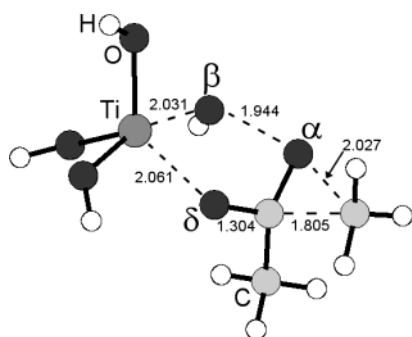


**Figure 15.** Optimized transition-state geometry for the rearrangement of the Ti(OH)<sub>3</sub>[OC(OOH)(CH<sub>3</sub>)<sub>2</sub>] chelated Criegee intermediate to produce the methyl acetate product via step 1 in Figure 14. (Bonds in the process of breaking or forming are shown with dashed lines; bond distances are in Å.)

titanium catalysts remains the Baeyer–Villiger rearrangement of the chelated Criegee intermediate (step 1, Figure 14). The activation barriers for this step are 3–4 kcal/mol lower for 2-methyl-3-pentanone than those for acetone because the electron-donating alkyl groups on the migrating  $\alpha$  carbon promote nucleophilic attack of the peroxo bond. The same trend is generally observed for Baeyer–Villiger oxidations with traditional peroxycarboxylic acid oxidants<sup>43–46</sup> and has also been

**TABLE 11. Reaction Energies and Activation Barriers for the Baeyer–Villiger Oxidation of 2-Methyl-3-pentanone with Hydrogen Peroxide via Mechanism II<sup>a</sup>**

figure	step	Ti				Sn			
		$\Delta E_R$	$\Delta G_R$	$\Delta E_A$	$\Delta G_A$	$\Delta E_R$	$\Delta G_R$	$\Delta E_A$	$\Delta G_A$
2	1	−9.9	1.3			−13.6	−2.5		
2	2	2.5	2.3	14.9	15.5	2.8	2.5	14.8	15.4
2	3	4.3	−5.2			11.3	1.1		
10	1	−1.7	10.5			−10.9	1.7		
10	2	−2.1	0.1	8.6	10.7	1.7	4.8	9.3	11.7
14	1	−74.5	−76.6	26.7	26.2	−78.5	−80.5	20.9	20.4
14	2	3.0	−9.7			8.7	−4.3		
$\Delta G_{\text{total}}^b$			35.2				28.0		

<sup>a</sup> All energies in kcal/mol. <sup>b</sup>  $\Delta G_{\text{total}}$  defined as the sum of the Gibbs activation barrier for the rate-determining step and the Gibbs reaction energies for all preceding quasi-equilibrated steps.

observed for platinum-catalyzed Baeyer–Villiger oxidations with hydrogen peroxide.<sup>47</sup> The relative reaction rates for tin and titanium can be estimated with the same definition of  $\Delta G_{\text{total}}$  used above; the values are reported in Table 11.

The overall reaction rate constants for Baeyer–Villiger oxidation of both acetone and 2-methyl-3-pentanone are much greater for tin catalysts than for titanium catalysts. The greater Lewis acidity of tin relative to that of titanium enhances adsorption of the ketone substrate on the metal active site and reduces the rate-determining activation barrier for the Baeyer–Villiger rearrangement of the chelated Criegee intermediate. The results obtained here indicate that intrinsic Baeyer–Villiger reaction rates for Ti(IV)–H<sub>2</sub>O<sub>2</sub> catalytic oxidation systems are approximately 5 orders of magnitude slower than reaction rates for analogous Sn(IV)–H<sub>2</sub>O<sub>2</sub> systems.

**Connection with Experimental Studies.** These calculations offer some insight into the selectivity differences observed by Corma and co-workers<sup>3–5</sup> for the oxidation of the unsaturated ketone dihydrocarvone with hydrogen peroxide using titanium- and tin-containing redox molecular sieve catalysts. Corma et al.<sup>3</sup> found that Sn- $\beta$  exclusively catalyzed the Baeyer–Villiger oxidation of dihydrocarvone while Ti- $\beta$  exclusively catalyzed its epoxidation. They also reported that Sn-MCM-41 provided only 68% lactone selectivity, with epoxidation representing the major side reaction.<sup>5</sup>

The computational results presented here indicate that tin activates hydrogen peroxide for epoxidation reactions just as readily as titanium, and Corma et al.'s experimental results for Sn-MCM-41 prove that tin-containing redox molecular sieves can act as epoxidation catalysts. Hence, the 100% Baeyer–Villiger selectivities obtained with Sn- $\beta$  are probably not the result of catalytic inactivity for epoxidation reactions with hydrogen peroxide. The Baeyer–Villiger reaction mechanism requires coordination of the ketone carbonyl group at the metal active site, whereas the epoxidation reaction requires no substrate coordination. The infrared experiments of Corma et al.<sup>3</sup> and our calculations both show that the ketone carbonyl moiety is much more likely to coordinate tin than titanium.

Coordination of the carbonyl moiety in dihydrocarvone places the double moiety far away from the metal active site (see Figure 1) and thereby prevents the epoxidation reaction with metal hydroperoxo species. In addition, the tin active sites are much more effective than the titanium ones at catalyzing the Baeyer–Villiger oxidation of coordinated ketones. These two factors combine to produce the remarkable chemoselectivity difference observed for Sn- $\beta$  and Ti- $\beta$ .

Mesoporous Sn-MCM-41 with its amorphous pore walls and high silanol densities should be much more hydrophilic than microporous, crystalline Sn- $\beta$ . Increased hydrophilicity of the molecular sieve framework will enable hydrogen peroxide and water to compete more effectively with the ketone substrate for access to the intraporous active sites. A reduction in the number of tin active sites available for ketone coordination will increase the frequency of the epoxidation reaction, which does not require substrate coordination, relative to the Baeyer–Villiger reaction. This effect might explain the reduced Baeyer–Villiger chemoselectivity observed for Sn-MCM-41 compared to Sn- $\beta$ .

## Conclusions

The mechanisms and performance of Ti(IV)–H<sub>2</sub>O<sub>2</sub> and Sn(IV)–H<sub>2</sub>O<sub>2</sub> catalytic oxidation systems have been compared for model epoxidation and Baeyer–Villiger reactions. The energetics calculated for the activation of hydrogen peroxide over tin catalysts are similar to the energetics calculated for titanium analogues. The greater Lewis acidity of tin compared to titanium reduces the activation barrier for the rate-determining step in both the epoxidation and Baeyer–Villiger reaction mechanisms. The overall reaction kinetics are similar for epoxidation processes using Ti(IV)–H<sub>2</sub>O<sub>2</sub> and Sn(IV)–H<sub>2</sub>O<sub>2</sub>. In the Baeyer–Villiger reaction, however, the Sn(IV)–H<sub>2</sub>O<sub>2</sub> oxidation system substantially outperforms the Ti(IV)–H<sub>2</sub>O<sub>2</sub> system. The results obtained from this study aid in understanding experimental results obtained previously for the oxidation of unsaturated ketones with titanium- and tin-containing redox molecular sieves.

**Acknowledgment.** We gratefully acknowledge the financial support of the National Science Foundation Training Grant (DGE-9554586) for the program “Catalysis for Environmentally Conscious Manufacturing” and funding received through a National Science Foundation Fellowship (R.R.S.). We also thank Dr. Frank A. Weinhold for helpful discussions.

## References and Notes

- (1) Arends, I. W. C. E.; Sheldon, R.; Wallau, M.; Schuchardt, U. *Angew. Chem., Int. Ed. Engl.* **1997**, *36*, 1145–1163.
- (2) Sheldon, R. A.; Wallau, M.; Arends, I. W. C. E.; Schuchardt, U. *Acc. Chem. Res.* **1998**, *31*, 485–493.
- (3) Corma, A.; Nemeth, L. T.; Renz, M.; Valencia, S. *Nature* **2001**, *412*, 423–425.
- (4) Renz, M.; Blasco, T.; Corma, A.; Fornés, V.; Jensen, R.; Nemeth, L. *Chem.–Eur. J.* **2002**, *8*, 4708–4717.
- (5) Corma, A.; Navarro, M. T.; Nemeth, L.; Renz, M. *Chem. Commun.* **2001**, 2190–2191.
- (6) Mal, N. K.; Bhaumik, A.; Ramaswamy, V.; Belhekar, A. A.; Ramaswamy, A. V. *Stud. Surf. Sci. Catal.* **1995**, *94*, 317–324.
- (7) Mal, N. K.; Ramaswamy, A. V. *J. Mol. Catal. A: Chem.* **1996**, *105*, 149–158.
- (8) Mal, N. K.; Ramaswamy, A. V. *Chem. Commun.* **1997**, 425–426.
- (9) Mal, N. K.; Ramaswamy, V.; Rakshe, B.; Ramaswamy, A. V. *Stud. Surf. Sci. Catal.* **1997**, *105*, 357–364.
- (10) Chaudhari, K.; Das, T. K.; Rajmohan, P. R.; Lazar, K.; Sivasanker, S.; Chandwadkar, A. J. *J. Catal.* **1999**, *183*, 281–291.
- (11) Bhaumik, A.; Kumar, P.; Kumar, R. *Catal. Lett.* **1996**, *40*, 47–50.
- (12) Watanabe, A.; Uchida, T.; Ito, K.; Katsuki, T. *Tetrahedron Lett.* **2002**, *43*, 4481–4485.
- (13) Sever, R. R.; Root, T. W. *J. Phys. Chem. B*, in press.
- (14) Bellussi, G.; Carati, A.; Clerici, M. G.; Maddinelli, G.; Millini, R. *J. Catal.* **1992**, *133*, 220–230.
- (15) Clerici, M. G.; Ingallina, P. *J. Catal.* **1993**, *140*, 71–83.
- (16) Lin, W.; Frei, H. *J. Am. Chem. Soc.* **2002**, *124*, 9292–9298.
- (17) Tozzola, G.; Mantegazza, M. A.; Ranghino, G.; Petrini, G.; Bordiga, S.; Ricchiardi, G.; Lamberti, C.; Zulian, R.; Zecchina, A. *J. Catal.* **1998**, *179*, 64–71.
- (18) Zecchina, A.; Bordiga, S.; Lamberti, C.; Ricchiardi, G.; Scarano, D.; Petrini, G.; Leofanti, G.; Mantegazza, M. *Catal. Today* **1996**, *32*, 97–106.
- (19) Sever, R. R.; Root, T. W. *J. Phys. Chem. B* **2003**, *107*, 4090–4099.
- (20) Frisch, M. J.; Trucks, G. W.; Schlegel, H. B.; Scuseria, G. E.; Robb, M. A.; Cheeseman, J. R.; Zakrzewski, V. G.; Montgomery, J. A., Jr.; Stratmann, R. E.; Burant, J. C.; Dapprich, S.; Millam, J. M.; Daniels, A. D.; Kudin, K. N.; Strain, M. C.; Farkas, O.; Tomasi, J.; Barone, V.; Cossi, M.; Cammi, R.; Mennucci, B.; Pomelli, C.; Adamo, C.; Clifford, S.; Ochterski, J.; Petersson, G. A.; Ayala, P. Y.; Cui, Q.; Morokuma, K.; Malick, D. K.; Rabuck, A. D.; Raghavachari, K.; Foresman, J. B.; Cioslowski, J.; Ortiz, J. V.; Stefanov, B. B.; Liu, G.; Liashenko, A.; Piskorz, P.; Komaromi, I.; Gomperts, R.; Martin, R. L.; Fox, D. J.; Keith, T.; Al-Laham, M. A.; Peng, C. Y.; Nanayakkara, A.; Gonzalez, C.; Challacombe, M.; Gill, P. M. W.; Johnson, B. G.; Chen, W.; Wong, M. W.; Andres, J. L.; Head-Gordon, M.; Replogle, E. S.; Pople, J. A. *Gaussian 98*, revision A.9; Gaussian, Inc.: Pittsburgh, PA, 1998.
- (21) Glendening, E. D.; Badenhop, J. K.; Reed, A. E.; Carpenter, J. E.; Bohmann, J. A.; Morales, C. M.; Weinhold, F. NBO 5.0. Theoretical Chemistry Institute: University of Wisconsin, Madison, WI, 2001.
- (22) Check, C. E.; Faust, T. O.; Bailey, J. M.; Wright, B. J.; Gilbert, T. M.; Sunderlin, L. S. *J. Phys. Chem. A* **2001**, *105*, 8111–8116.
- (23) Weinhold, F. A. *Encyclopedia of Computational Chemistry*. John Wiley & Sons: New York, 1998.
- (24) Alba, M. D.; Luan, Z.; Klinowski, J. *J. Phys. Chem.* **1996**, *100*, 2178–2182.
- (25) Blasco, T.; Corma, A.; Navarro, M. T.; Pariente, J. P. *J. Catal.* **1995**, *156*, 65–74.
- (26) Blasco, T.; Camblor, M. A.; Corma, A.; Esteve, P.; Guil, J. M.; Martínez, A.; Perdigón-Melón, J. A.; Valencia, S. *J. Phys. Chem. B* **1998**, *102*, 75–88.
- (27) Corma, A.; García, H.; Navarro, M. T.; Palomares, E. J.; Rey, F. *Chem. Mater.* **2000**, *12*, 3068–3072.
- (28) Lamberti, C.; Bordiga, S.; Arduino, D.; Zecchina, A.; Geobaldo, F.; Spanó, G.; Genoni, F.; Petrini, G.; Carati, A.; Villain, F.; Vlaic, G. *J. Phys. Chem. B* **1998**, *102*, 6382–6390.
- (29) Le Noc, L.; On, D. T.; Solomykina, S.; Echchahed, B.; Béland, F.; dit Moulin, C. C.; Bonnevot, L. *Stud. Surf. Sci. Catal.* **1996**, *101*, 611–620.
- (30) Notari, B. *Adv. Catal.* **1996**, *41*, 253–334.
- (31) Prakash, A. M.; Sung-Suh, H. M.; Kevan, L. *J. Phys. Chem. B* **1998**, *102*, 857–864.
- (32) Mal, N. K.; Ramaswamy, V.; Ganapathy, S.; Ramaswamy, A. V. *Chem. Commun.* **1994**, 1933–1934.
- (33) Mal, N. K.; Bhaumik, A.; Kumar, R.; Ramaswamy, A. V. *Catal. Lett.* **1995**, *33*, 387–394.
- (34) Mal, N. K.; Ramaswamy, V.; Rajamohan, P. R.; Ramaswamy, A. V. *Microporous Mater.* **1997**, *12*, 331–340.
- (35) Boccuti, M. R.; Zecchina, A.; Leofanti, G.; Petrini, G. *Stud. Surf. Sci. Catal.* **1989**, *48*, 133–144.
- (36) Gonzalez, C.; Schlegel, H. B. *J. Chem. Phys.* **1989**, *90*, 2154–2161.
- (37) Neurock, M.; Manzer, L. E. *Chem. Commun.* **1996**, 1133–1134.
- (38) Tantanak, D.; Vincent, M. A.; Hillier, I. H. *Chem. Commun.* **1998**, 1031–1032.
- (39) Yudanov, I. V.; Gisdakis, P.; Valentin, C. D.; Rösch, N. *Eur. J. Inorg. Chem.* **1999**, 2135–2145.
- (40) Bach, R. D.; Glukhovtsev, M. N.; Gonzalez, C. *J. Am. Chem. Soc.* **1998**, *120*, 9902–9910.
- (41) Deubel, D.; Sundermeyer, J.; Frenking, G. *Eur. J. Inorg. Chem.* **2001**, 1819–1827.
- (42) Gisdakis, P.; Yudanov, I. V.; Rösch, N. *Inorg. Chem.* **2001**, *40*, 3755–3765.
- (43) Bolm, C. *Adv. Catal. Processes* **1997**, *2*, 43–68.
- (44) Krow, G. R. *Org. React.* **1993**, *43*, 251–798.
- (45) Renz, M.; Meunier, B. *Eur. J. Org. Chem.* **1999**, 737–750.
- (46) Strukul, G. *Angew. Chem., Int. Ed.* **1998**, *37*, 1198–1209.
- (47) Gavagnin, R.; Cataldo, M.; Pinna, F.; Strukul, G. *Organometallics* **1988**, *17*, 661–667.